A Frequency-Switching Inductive Power Transfer System for Wireless, Miniaturised and Large-Scale Neural Interfaces

Gian Luca Barbruni, *Graduate Student Member, IEEE,* Claudia Cordara, Marco Carminati, *Senior Member, IEEE,* Sandro Carrara, *Fellow, IEEE,* and Diego Ghezzi, *Senior Member, IEEE*

***Abstract*—Three-coil inductive power transfer is the state-of-the-art solution to power multiple miniaturised neural implants. However, the maximum delivered power is limited by the efficiency of the powering link and safety constrains. Here we propose a frequency-switching inductive link, where the passive resonator normally used in a three-coil link is replaced by an active resonator. It receives power from the external transmitter via a two-coil inductive link at the low frequency of 13.56 MHz. Then, it switches the operating frequency to the higher frequency of 433.92 MHz through a dedicated circuitry. Last, it transmits power to 1024 miniaturised implants via a three-coil inductive link using an array of 37 focusing resonators for a brain coverage of 163.84 mm^2. Our simulations reported a power transfer efficiency of 0.013$\%$ and a maximum power delivered to the load of 1970 μW under safety-constrains, which are respectively two orders of magnitude and more than six decades higher compared to an equivalent passive three-coil link. The frequency-switching inductive system is a scalable and highly versatile solution for wireless, miniaturised and large-scale neural interfaces.**

***Index Terms*—Inductive Power Transfer; Implantable Medical Device; Neural Interfaces; Brain-Machine Interfaces.**

Manuscript received Month X, 2023; revised Month X, 2023; accepted Month X, 2023. Date of publication Month X, 2023; date of current version Month X, 2023.

Corresponding author: Diego Ghezzi.

Gian Luca Barbruni is with Bio/CMOS Interfaces Laboratory (BCI), École Polytechnique Fédérale de Lausanne, 2000 Neuchâtel, Switzerland and with Medtronic Chair in Neuroengineering, École Polytechnique Fédérale de Lausanne, 1202 Geneva, Switzerland. (e-mail: gianluca.barbruni@epfl.ch)

Claudia Cordara was with Bio/CMOS Interfaces Laboratory (BCI), École Polytechnique Fédérale de Lausanne, 2000 Neuchâtel, Switzerland and also with Dipartimento di Elettronica, Informazione e Bioingegneria, Politecnico di Milano, 20133 Milan, Italy. (e-mail: claudia.cordara@mail.polimi.it)

Marco Carminati is with Dipartimento di Elettronica, Informazione e Bioingegneria, Politecnico di Milano, 20133 Milan, Italy. (e-mail: marco1.carminati@polimi.it)

Sandro Carrara is with Bio/CMOS Interfaces Laboratory (BCI), École Polytechnique Fédérale de Lausanne, 2000 Neuchâtel, Switzerland. (e-mail: sandro.carrara@epfl.ch)

Diego Ghezzi is with Medtronic Chair in Neuroengineering, Center for Neuroprosthetics and Institute of Bioengineering, School of Engineering, École Polytechnique Fédérale de Lausanne, 1202 Geneva, Switzerland and with Ophthalmic and Neural Technologies Laboratory, Department of Ophthalmology, University of Lausanne, Hôpital ophtalmique Jules-Gonin, Fondation Asile des Aveugles, 1002 Lausanne, Switzerland (e-mail: info@ghezzilab.org)

Color versions of one or more of the figures in this article are available online at https://ieeexplore.ieee.org.

Digital Object Identifier 10.1109/TBCAS.2023.XXXXXXX

I. Introduction

WIRELESS, miniaturised and large-scale neural interfaces are emerging neurotechnologies [1], [2]. Their development is based on the observation that advanced prostheses, compensating for the loss or the impairment of diverse human functions, will require nearly single-cell resolution, thus employing dense spatial and temporal sampling across multiple cortical areas in all three dimensions [2]. Inductive Power Transfer (IPT) has been identified as optimal wireless technology to power multiple neural implants at the same time [3]. However, the maximum power transmitted by an IPT link is limited by the maximum averaged Specific Adsorption Rate (SAR) defined by safety standards [4], [5]: for the human head, it is set by the US Federal Communications Commission to 1.6 W/kg for 1 g of tissue mass measured during 30 minutes of exposure [6]. Specifically, the SAR is defined as in (1):

$$SAR = \frac{\sigma |E_{rms}|^2}{\rho} \tag{1}$$

where σ and ρ are respectively the tissue conductivity and density and E_{rms} is the round value of the electric field, whose gradient is derived from Maxwell's equation as in (2):

$$\nabla \times E = -\frac{\partial B}{\partial t} \propto fI \tag{2}$$

where B is the magnetic field, f is the operating frequency and I is the flowing current. The SAR is proportional to $(fI)^2$ [7]. Hence, decreasing f is necessary to reduce the SAR.

On the other hand, f is lower limited by the receiver (Rx) lateral size. As a rule of thumb, f should be higher than a few hundreds of MHz to match the Rx lateral size (i.e., $<$ 1 mm) and lower than a few GHz to limit the tissue losses [8]. The maximum Power Delivered to the Load (PDL) within the SAR limit (SAR-constrained PDL) is limited by the link efficiency, which is usually very small for a miniaturised Rx (i.e., lateral size $<$ 1 mm) [4]. Hence both the transmitted power and the PDL are SAR-limited [4].

Multiple high-frequency IPT links have been proposed to power miniaturised implants. Microbeads exploits a two-coil IPT link to power a single 300 $\times$ 300 μm^2 Rx at 1.18 GHz obtaining a PDL of 55.5 μW for a SAR of 30.6 W/kg [9]. A three-coil IPT link, which includes a passive resonator, can be used to increase the PDL by almost one order of magnitude [5]. Additionally, since the magnetic field is increased in the

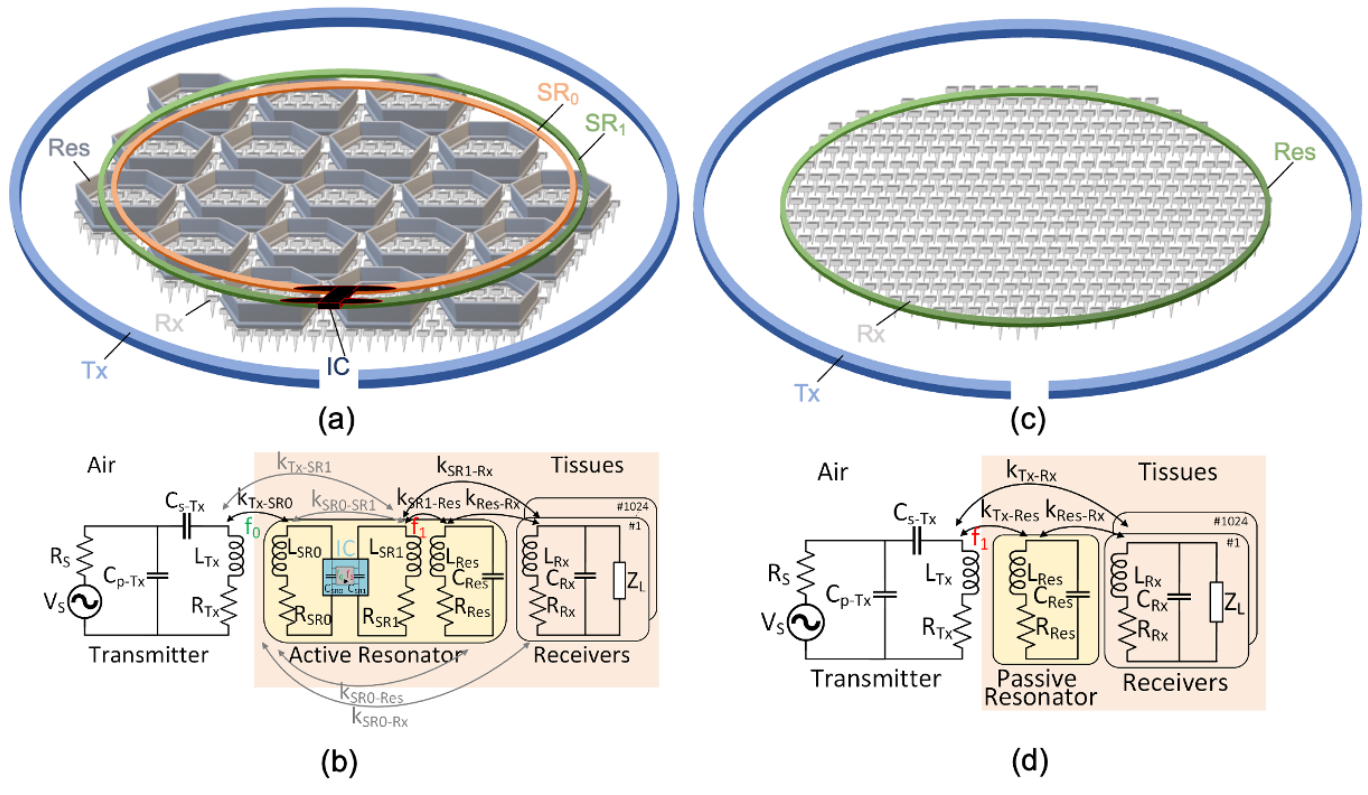

Figure 1. (a) Sketch of the FS-IPT link highlighting the Tx in blue, the active resonator (SR_0 in orange, SR_1 in green, the CMOS IC for frequency switching in black, and the array of focusing passive coils Res in dark grey) and 1024 Rx chips in light grey. (b) Simplified equivalent circuit of the FS-IPT link including the source power (V_S, R_S), the perfectly matched Tx (L_{Tx}, R_{Tx}, C_{s-Tx}, C_{p-Tx}) coupled with SR_0 (L_{SR0}, R_{SR0}) via k_{Tx-SR0} and operating at f_0, the CMOS IC for switching the operating frequency from the lower f_0 to the higher f_1, SR_1 (L_{SR1}, R_{SR1}) coupled with one Res (L_{Res}, R_{Res}) via $k_{SR1-Res}$ and with 1024 Rx chips (L_{Rx}, R_{Rx}) matched at Z_L through C_{Rx} via k_{SR1-Rx} and operating at f_1. (c) Sketch of the passive three-coil IPT link highlighting the Tx in blue, the passive resonator Res in green and 1024 Rx chips in light grey. (d) Simplified equivalent circuit of the passive three-coil IPT link including the source power (V_S, R_S); the perfectly matched Tx (L_{Tx}, R_{Tx}, C_{s-Tx}, C_{p-Tx}) coupled with the passive Res (L_{Res}, R_{Res}) via k_{Tx-Res} and 1024 Rx chips (L_{Rx}, R_{Rx}) matched at Z_L through C_{Rx}, coupled with Res via k_{Res-Rx} and operating at the high f_1.

near region of the passive resonator, the three-coil IPT link allows similar PDL to each Rx located in the area covered by the passive resonator. Neurograins exploits a three-coil IPT link toward multiple 500 $\times$ 500 μm^2 receivers operating at 915 MHz and obtaining a PDL of 235 μW for a SAR of 19.6 W/kg [10]. However, the maximum SAR is well beyond the safety limit in both approaches. Hence, duty cycling the power transmission is necessary, although limiting the system operation. Another solution consists of a two-tier hierarchy of near-field inductively coupled links [11]. The structure allows for an uniform energy distribution to mm-scale neural implants. However, the operating frequency remains high due to the small Rx lateral size. Hence, the SAR is still the main limiting factor. Also, the transcranial cable is a sub-optimal solution, since it might lead to post-operative complications [12]. An hybrid inductive-ultrasonic link has also been proposed [13], exploiting the less stringent safety limit of Acoustic Power Transfer (APT) for the back-end wireless transmission [3]. However, simultaneously powering multiple devices via APT is challenging due to acoustic focalization and beamforming limitations [3]. Therefore, there is a need for a safe, efficient and scalable wireless link to enable miniaturised and large-scale neural interfaces.

Here we introduce a Frequency-Switching (FS) inductive link. Compared to a passive three-coil IPT link, the passive resonator is transformed into an active resonator. The system increases the SAR-constrained PDL allowing wireless powering of multiple, miniaturised and large-scale neural implants. Results show that the FS-IPT link outperforms a passive three-coil IPT link while powering the smallest neural Rx in literature.

II. Operational Principles and Resonator Design

Figure 1(a) shows a sketch of the FS-IPT link, in which the power transmission is divided into two serial links resonating at different frequencies. Figure 1(b) highlights the FS-IPT electrical equivalent circuit. The active resonator is composed of: i) a receiver SR_0, modelled with inductance L_{SR0} and series resistance R_{SR0} resonating at the low operating frequency f_0 and coupled to the Tx through the coupling

coefficient k_{Tx-SR0}; ii) a transmitter SR_1, modelled with inductance L_{SR1} and series resistance R_{SR1} resonating at the high operating frequency f_1; iii) an array of N passive resonators (Res), each modelled with inductance L_{Res} and series resistance R_{Res} resonating at f_1 via C_{Res} and iv) a circuit for matching SR_0 and SR_1 at f_0 and f_1 respectively through C_{SR0} and C_{SR1} and for switching the operating frequency from f_0 to f_1. The source power P_S is generated by the power amplifier modelled by V_S and R_S (R_S = 50 Ω) and transmitted to SR_0. Tx and SR_0 (respectively the blue and orange coils in Figure 1(a)) work as a two-coil IPT link operating at the low frequency f_0=13.56 MHz. Tx is modelled with inductance L_{Tx} and series resistance R_{Tx} and it resonates at f_0 through the impedance matching network composed by C_{s-Tx} and C_{p-Tx}.

The PDL_0 of this two-coil link is approximated as in (3) [3]:

$$PDL_0(\omega) \approx \frac{V_S^2}{2R_{Tx}} \cdot \frac{k_{Tx-SR0}^2 Q_{Tx} Q_{SR0L}}{(1+k_{Tx-SR0}^2 Q_{Tx} Q_{SR0L})^2} \cdot \frac{Q_{SR0L}}{Q_L} \tag{3}$$

Instead, SR_1, Res and Rx operate at the high-frequency f_1, which is fixed by the Rx size (f_1 = 433.92 MHz for D_{oRx}= 200 μm). Since the minimum required resonator area is 163.84 mm^2 for 1024 implants, SR_1 (green coil in Figure 1(a)) is a single turn coil to avoid Self Resonance Frequency (SRF) degradation at f_1.

The array of 37 focusing Res (dark grey coils in Figure 1(a)) allows an almost uniform power delivery to the entire area of coverage of SR_1. In this configuration each Res_i differently contributes to the PDL_1 of the high-frequency IPT link, as approximated in (4):

$$PDL_1(\omega) \approx \sum_{i=1}^{N} \frac{V_S^2}{2R_{Tx}} \cdot \frac{(k_{SR1-Res,i}^2 Q_{SR1} Q_{Res,i}) \cdot (k_{Res,i-Rx}^2 Q_{Res,i} Q_{RxL})}{(1+k_{SR1-Res,i}^2 Q_{SR1} Q_{Res,i} + k_{Res,i-Rx}^2 Q_{Res,i} Q_{RxL})^2} \cdot \frac{Q_{RxL}}{Q_L} \tag{4}$$

In this complex scenario, different undesired inter-couplings (grey couplings in Figure 1(b)) arise from the co-planar SR_0 and SR_1, such as $k_{Tx-SR1} \simeq k_{Tx-SR0}$, $k_{SR0-Res} \simeq k_{SR1-Res}$, $k_{SR0-Rx} \simeq k_{SR1-Rx}$ and $k_{SR0-SR1} \approx$ 0.5-1. However, these inter-couplings are among resonant to non-resonant coils (i.e., coils resonating at different operating frequencies) and, therefore, their influence has not been considered in (3) and (4) [14]. The total Power Transfer Efficiency (PTE) of the FS-IPT link is calculated as in (5):

$$PTE = PTE_0 \cdot \eta_{IC} \cdot PTE_1 \tag{5}$$

where PTE_0 and PTE_1 are respectively derived from (3) and (4) as in [3] and η_{IC} is the efficiency of the CMOS IC for switching the operating frequency from f_0 to f_1. It is worth noting that, in this work, the CMOS IC is not fabricated but only simulated. This circuit does not introduce any criticality in area or power consumption, and it can be designed based on state-of-the-art blocks. Therefore, it is not the core of this research. The Rx, modelled with inductance L_{Rx}, series resistance R_{Rx} and matched at f_1 with the parallel capacitor C_{Rx} for the load Z_L, is identical for the FS-IPT link and the passive three-coil IPT link (Figure 1(c)). It means that available optimisation algorithms can be used to optimise the miniaturised Rx and to select the optimal operating frequency f_1 [5], [15], [16].

The FS-IPT link is compared to a passive three-coil IPT link. In its electrical equivalent model (Figure 1(d)), the passive resonator coil (Res), modelled by its inductance L_{Res} and series resistance R_{Res} and resonating at f_1 through the parallel capacitor C_{Res}, shares the same geometrical design of SR_1 in the FS-IPT (limited by the SRF). The passive resonator is magnetically coupled at the same f_1 = 433.92 MHz to both the Rx via k_{Res-Rx} and the Tx via k_{Tx-Res}.

The key advantage of the FS-IPT link is using different frequencies for the two transmissions. Both active and passive resonators are placed in proximity to the Rx ($\simeq$ 14 mm deep). This penetration depth is close to the Tx-Rx distance d_{Tx-Rx} in a passive three-coil IPT link operating at f_1. In particular, referring to the electrical equivalent circuit of Figure 1(d), the PDL for a passive three-coil IPT link is calculated as in (6) [3]:

$$PDL(\omega) = \frac{V_S^2}{2R_{Tx}} \cdot \frac{(k_{Tx-Res}^2 Q_{Tx} Q_{Res}) \cdot (k_{Res-Rx}^2 Q_{Res} Q_{RxL})}{(1+k_{Tx-Res}^2 Q_{Tx} Q_{Res} + k_{Res-Rx}^2 Q_{Res} Q_{RxL})^2} \cdot \frac{Q_{RxL}}{Q_L} \tag{6}$$

In the FS-IPT link, the same distance is covered at f_0 (Tx-SR_0). For the same value of SAR, using f_0 = 13.56 MHz instead of f_1 = 433.92 MHz results in a theoretical $\times$1024 gain for the flowing current I^2, as from (1) and (2). In other words, for the same transmitted power, the same source impedance R_S and a perfectly matched network, the maximum SAR is reduced by a factor of 1024. Also, the limiting link in terms of SAR-constrained PDL is the one among SR_1-Res-Rx, as the operating frequency is again f_1. However, since the active resonator is implanted close to the Rx, the high-frequency transmission travels for less than one millimiter (SR_1-Rx). Hence, both k_{SR1-Rx} and the maximum PTE increase [17]. Moreover, the presence of N passive focusing Res_i further increase the PDL_1 as in (4), being each Res_i coupled with both SR_1 via $k_{SR_1-Res,i}$ and Rx via $k_{Res,i-Rx}$ and intrinsically exploiting the known advantages of a three-coil link.

III. Materials and Methods

The FS-IPT link and the passive three-coil IPT link were both designed and optimised in ANSYS HFSS®.

An 8-layer human head model composed of skin (1.5 mm), fat (1.5 mm), muscle (2.5 mm), skull (6.5 mm), dura mater (1 mm), CerebroSpinal Fluid (CSF), pia mater (0.1 mm) and brain (20 mm) was used [9] (Figure 2(a)). Both the passive resonator (passive three-coil IPT link) and the active resonator (FS-IPT link) were characterised and optimised when implanted in epidural (Figure 2(b)) or in subdural position (Figure 2(c)). The CSF thickness is different for the two models.

For an epidural resonator, the CSF thickness is equal to the thickness of the Rx (Figure 2(b)). For a subdural resonator, it is equal to the thickness of the Rx plus the resonator itself (Figure 2(c)). The pia mater was modelled with the same electrical properties of the CSF [18]. Frequency-dependent electrical properties and thicknesses of all the tissues were derived from [18] and [19] respectively.

This study evaluates powering 1024 miniaturised Rx chips at the same time (Rx_1, Rx_2 ... Rx_n in Figure 2), implanted with a pitch of 400 μm (replicating the Utah array [20]). Hence, 1024 Rx chips cover a total surface of 163.84 mm^2. The Rx was designed and optimized as in [5] and the optimal operating frequency of 433.92 MHz was selected also considering all the design constrains related to a CMOS-integrated planar spiral coil where the Rx is directly fabricated using the ultra-thick top-metal layer of the CMOS technology (TSMC-180nm, 20 kA flavour). Therefore, the Rx is a squared 2 μm-thick aluminium planar spiral coil with the up-to-date smallest outer diameter D_{oRx} = 200 μm, 13 turns with trace width and spacing respectively of 2 μm and 1.5 μm (satisfying the CMOS design rule check) integrated on a 300 μm-thick silicon substrate and insulated with a 1 μm-thick layer of SiO_2.

For the optimized active resonator (FS-IPT) of Figure 2(d), SR_0 is a single turn circular copper coil with outer diameter of 13.5 mm, trace width of 500 μm and thickness of 18 μm. SR_0 is coupled with the Tx which is a two-turns circular copper coil with outer diameter of 16 mm, trace width of 1.5 mm, spacing of 1 mm and thickness of 50 μm integrated in a standard 1.5 mm-thick FR4. SR_1 is a circular copper coil with outer diameter of 14.7 mm, trace width of 60 μm and thickness of 18 μm, and it is designed co-planar to SR_0. Each Res is single turn hexagonal copper coil with radius of 1.2 mm, trace width of 100 μm and thickness of 35 μm. The entire active resonator cross-section is shown in Figure 2(f) as multi-layer of polyimide (PI)-Cu-PI-Cu-PI with thicknesses of 150-18-80-35-25 μm, respectively. For the optimized passive resonator (three-coil IPT) of Figure 2(e), Res is geometrically identical to SR_1, sandwiched between two 145 μm-thick PI layers (Figure 2(g)) and coupled at f_1 = 433.92 MHz with the Tx, which is a single turn circular copper coil with diameter of 20 mm, trace width of 3 mm and thickness of 18 μm integrated in a standard 1.5 mm-thick FR4.

The resonators (passive and active) were laid out in Altium Designer® and fabricated in flexible PI technology (PCBWay). The external transmitters (Tx) were fabricated with standard rigid PCB technology and FR4-substrate (PCBWay). Each coil constituting the FS-IPT was characterised both in air and ex-vivo. In the ex-vivo setup, a 14 mm-thick beef is interposed among the Tx and the active resonator which is placed above a 50 mm-thick beef. Coil characterisation was performed with the vector network analyser (ZVL, Rohde&Schwarz) after standard short-open-load calibration.

The CMOS IC for the frequency switching was designed, simulated and optimized in Cadence® Virtuoso IC6.1.7 using TSMC-180nm BCD technology.

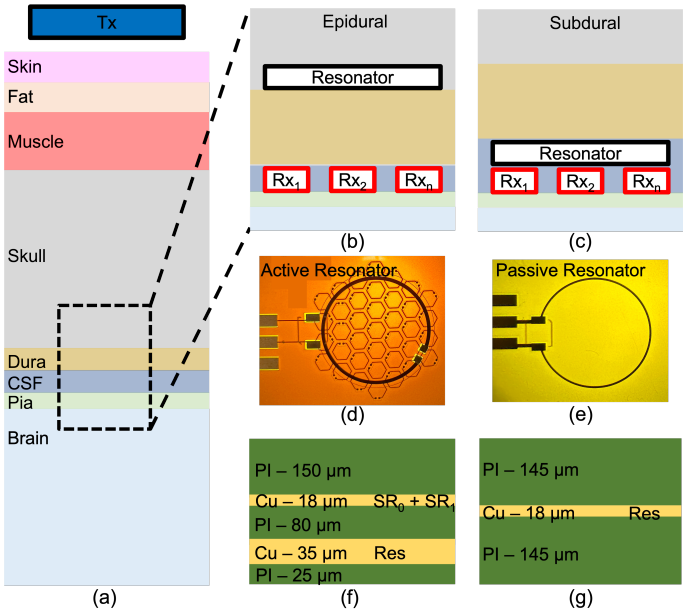

Figure 2. (a) Realistic 8-layer model including skin, fat, muscle, skull, dura mater, CSF, pia mater and brain. Section model for an epidural (b) and a subdural (c) resonator implant. (d-g) Top-view image and cross-section sketch respectively of the fabricated active (d), (f) and passive resonator (e), (g).

IV. Results

A. FS-IPT Simulation and Optimization

First, we simulated the performance of the FS-IPT link as a function of several design parameters (Figure 3). From a surgical point of view the resonator can be implanted in epidural (Figure 2(b)) or subdural position (Figure 2(c)). Figure 3(a) shows the simulated SAR-constrained PDL variation as a function of the active resonator encapsulation thickness for an epidural (black) and a subdural (grey) implant. The subdural implant outperforms the epidural one for any encapsulation thickness. Indeed, the resonator is optimised when it is co-planar with the Rx since its quality factor Q makes the PDL to increase [21]. If the active resonator is implanted in epidural position, the relative distance to the Rx increases, and its influence on the magnetic field at the Rx plane is reduced. Q is also influenced by the thickness of the total encapsulation [22] since a thicker layer improves EM radiation. On the other hand, a thinner encapsulation makes the implant more conformable to the cortical surface [23]. As a rule of thumb, the optimal encapsulation thickness is a trade-off among efficiency (the higher the better) and surgical invasiveness (the lower the better). Figure 3(b) shows the relative SAR-constrained PDL variation as a function of the thickness for two materials: polydimethylsiloxane (PDMS) and PI. For both materials, when the encapsulation increases from 200 μm to 300 μm a 3-4$\times$ gain is visible. A further increase in thickness does not produce any further improvement, since the relative distance between the resonator and the Rx linearly increases with the encapsulation thickness. An inflection point is present at 550 μm. Overall, PDMS shows a higher SAR-constrained

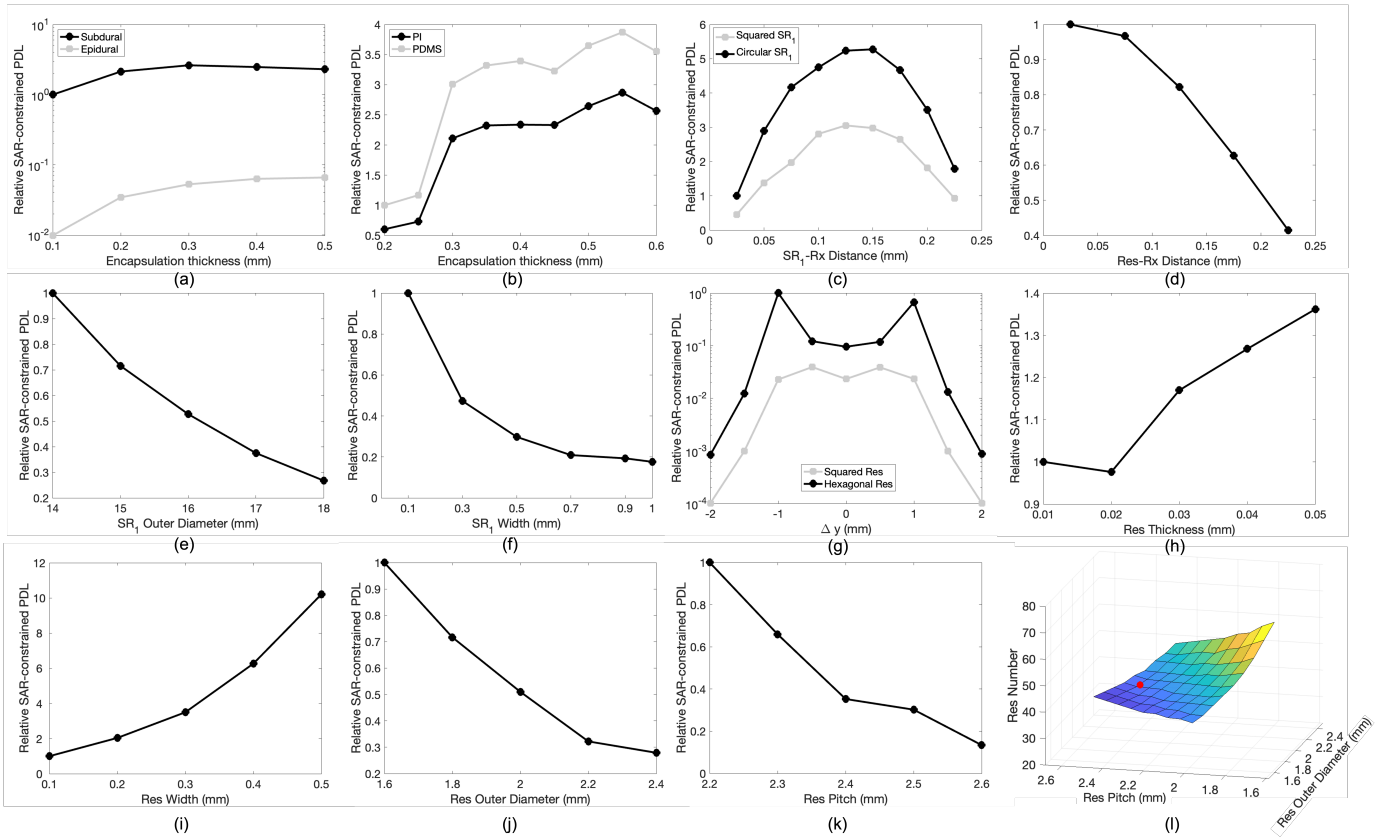

Figure 3. Relative simulated SAR-constrained PDL variation as a function of the active resonator total encapsulation thickness for an epidural (grey) and a subdural (black) implant (a), the active resonator encapsulation thickness for PI (black) and PDMS (grey) encapsulations (b), the SR_1 position (SR_1-Rx distance) for a squared (grey) and circular (black) SR_1 shape (c), the Res position (Res-Rx distance) (d), the SR_1 outer diameter (e), and SR_1 trace width (f). Relative simulated SAR-constrained PDL variation as a function of (g) the Rx lateral misalignment within a single squared (grey) and hexagonal (black) Res; (h) the Res trace thickness; (i) the Res trace width; (j) the Res outer diameter and (k) the Res pitch. (l) 3-D graph of the required number of Res as a function of both the Res outer diameter and pitch. The red circle highlights 37 Res as optimal trade-off used in this work.

PDL than PI, which is ideal since PDMS has also lower bending stiffness and higher conformability than PI.

In the following results, we considered a PI-based 300 μm-thick subdural active resonator. We selected PI, instead of PDMS, so the active resonator could be manufactured by a commercial partner. We then investigated the relative position of both SR_1 and Res. SR_1 shows its optimal performance when placed in the center of the sandwitch (Figure 2(f)) corresponding to a SR_1-Rx distance of 140 μm (Figure 3(c)). As reference, a circular coil (black) shows a 2$\times$-improvement compared to a squared one (grey). On the contrary, for the Res-Rx relative position, the performance increases for a Res implanted near to the Rx (Figure 3(d)), therefore, for a thin coating (25 μm of PI) and a thick substrate (PI-Cu-PI of 150-18-80 μm, Figure 2(f)). The theoretical optimal position for a passive resonator is co-planar with the Rx so, the smaller the Res-Rx distance, the higher the SAR-constrained PDL. For a circular SR_1, increasing the outer diameter reduces the PDL (Figure 3(e)). Increasing the SR_1 outer diameter from 14 mm to 18 mm result in an almost 10$\times$ PDL decrease. The smaller SR_1 diameter (14 mm) is fixed by the number of powered implant at the same time (1024 receivers with a pitch of 400 μm). A similar 10$\times$ PDL decrease is observed when increasing the SR_1 trace width from 0.1 mm to 1 mm (Figure 3(f)) since the fill factor is reduced. As a consequence, both the coil inductance and the Q at high-frequency decrease accordingly.

For the Res optimization, hexagonal Res show an order of magnitude increase in the total SAR-constrained PDL compared to squared Res (Figure 3(g)) for an Rx moved along a single Res area (symmetrically from -2 mm outside the Res to perfectly in the center of the Res at 0 mm). Figure 3(h), (i) respectively show the relative SAR-constrained PDL variation as a function of the Res trace thickness and width. Both parameters increase the maximum PDL.

When optimising the FS-IPT, three main regions are considered for the Rx; corresponding to the area inside each Res (1), below the traces of each Res (2) and outside all the Res (3). The three regions are shown in Figure 4(a). A uniform power distribution depends on the optimisation of the Res width, diameter and pitch (Figure 3(i), (j), (k) respectively). If Res outer diameter increases, the PDL of the Rx located in region

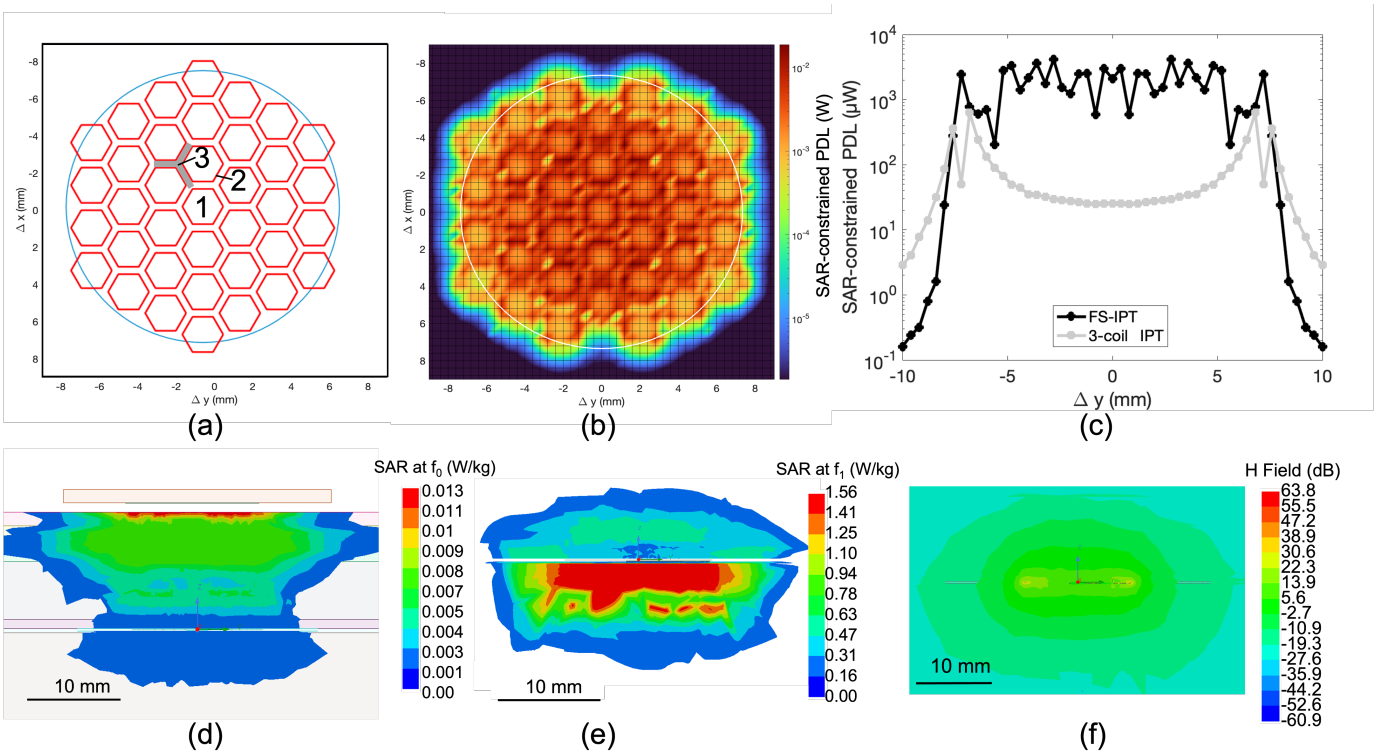

Figure 4. (a) Geometrical distribution of the 37 hexagonal focusing Res inside the circular SR_1 covering 1024 wireless Rx chips distributed within three different regions: inside Res (1), under the Res trace (2) and outside Res (3). (b) Color-plot of the maximum SAR-constrained PDL in the entire area of coverage of SR_1. (c) SAR-constrained PDL comparison among the simulated standard three-coil IPT (grey) and the novel FS-IPT link (black) as a function of the Rx lateral misalignment respectively along Res (three-coil) and SR_1 (FS-IPT). Quantitative SAR analysis (d) for the low frequency link at f_0 among Tx and SR_0 and (e) for the high frequency link at f_1 among SR_1, Res and Rx. (f) Magnetic field magnitude for the high-frequency link at f_1 among SR_1, Res and Rx.

1 decreases. Similarly, the PDL of the Rx located in region 3 decreases when Res pitch increases. At the same time, when Res trace width decreases the Rx located in region 2 under the trace receive less power. On the other hand, decreasing both Res outer diameter and pitch exponentially increases the number of Res required to cover the SR_1 area (Figure 3(l)). For example, 77 Res are necessary for the smallest Res outer diameter of 1.6 mm and the smallest pitch of 1.6 mm while only 27 Res are needed for the highest Res outer diameter of 2.4 mm and the highest pitch of 2.6 mm. Similarly, thicker and wider Res traces might increase the rigidity of the system. Therefore, using 37 Res (red marker of Figure 3(l)) is a compromise among Res diameter, pitch, maximum PDL, uniform power distribution in the three regions and mechanical rigidity of the active implant.

Figure 4(a) shows the in-scale geometrical distribution of the 37 focusing Res (red) covering 1024 Rx chips with a pitch of 400 μm implanted inside the circular SR_1 (blue). Figure 4(b) shows the color-plot of the maximum SAR-constrained PDL when distributing the Rx in the area of coverage of SR_1. The color distribution shows an almost uniform power distribution under the SR_1 area, with a peak power of 2100 μW and an average power of 1970 μW. Indeed, the three powering regions 1, 2, 3 in Figure 4(a) are characterised by a slightly different PDL. It is worth mentioning that the Res centered in (7;0) is not active as located below the exciting lumped port of SR_1. Therefore, Rx chips underneath receive negligible power. Being the plot symmetrically constructed by simulating the lower-right quadrant, the same identical condition is replicated for the Rx chips underneath the Res centered in (-7;0). This situation is a simulation-related problem not occurring in a physical implementation. Figure 4(c) shows the comparison of the maximum SAR-constrained PDL for the three-coil IPT link (grey) and the FS-IPT link (black). The plot shows the maximum PDL variation toward Rx lateral misalignment along the entire Res area (three-coil IPT) and SR_1 area (FS-IPT) while moving the Rx from (0;-9) to (0;9). The semi-logarithmic comparative simulation highlights that for the same miniaturised Rx, the averaged SAR-constrained PDL_1 of (4) for the FS-IPT link is more than six decades higher than the PDL of (6) for a passive three-coil IPT link. When multiple co-planar Res are simultaneously activated by SR_1, their flowing current is in phase. Therefore, the Rx chips located in region 3 receive lower magnetic field, as visible from both the SAR-constrained PDL color-plot in Figure 4(b) and the decreasing PDL peaks in Figure 4(c) which are occurring in between different Res (region 3).

Figures 4(d), (e) respectively show the local SAR field

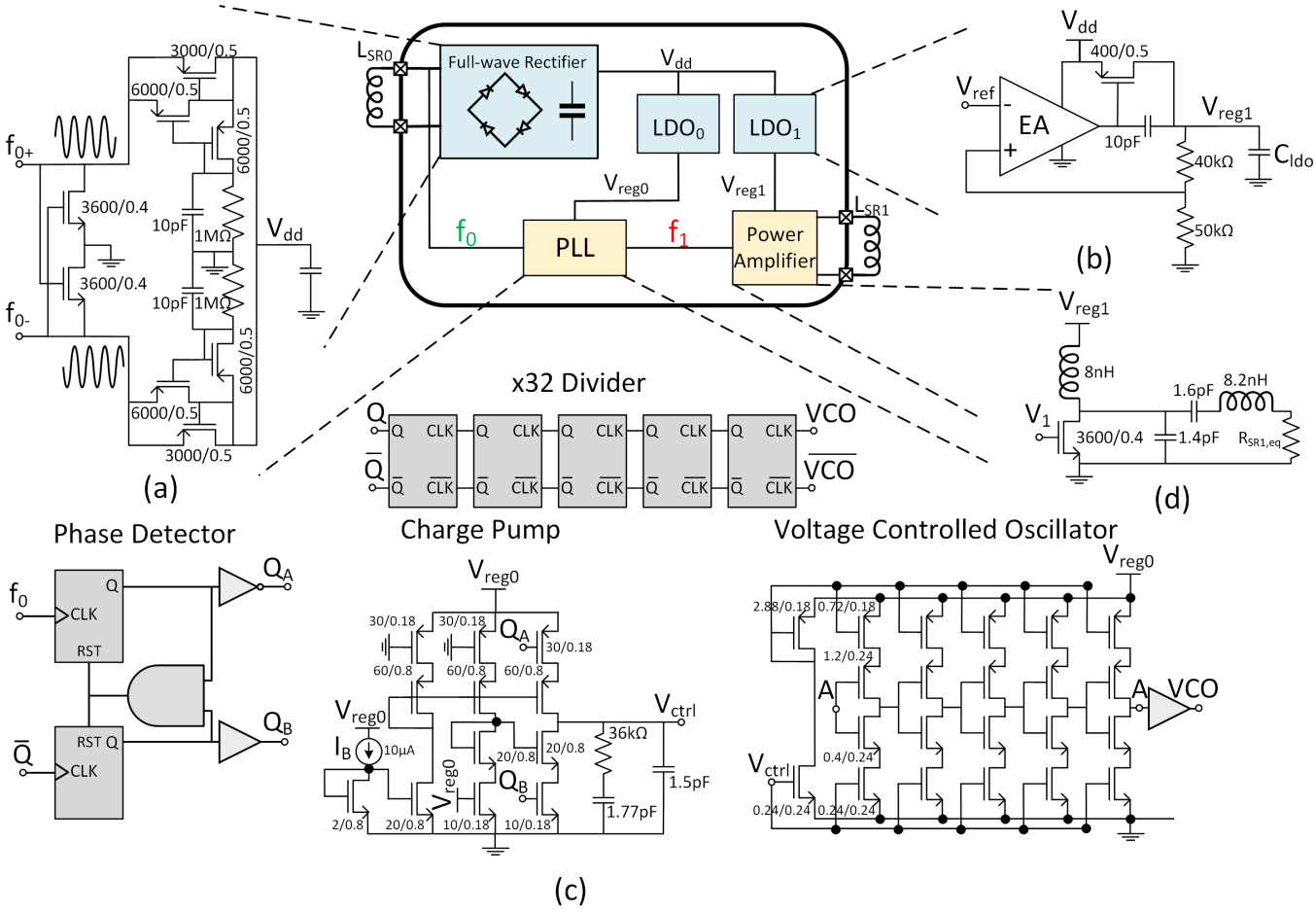

Figure 5. Schematic of the wireless CMOS IC for the frequency switching from f_0 to f_1 including: (a) full-wave passive rectifier, (b) LDOs, (c) PLL and (d) class-E power amplifier.

distribution in the ZY plane cut at the origin for the low frequency link at f_0 and for the high frequency link at f_1 highlighting that the maximum SAR (respectively at skin and brain levels for the two transmissions) is below the maximum allowable value of 1.6 W/kg. Figure 4(f) shows the H-field magnitude in the area covered by SR_1.

Figure 5 highlights the main circuits of the CMOS IC responsible for the frequency switching, including the Power Management Unit (PMU, blue) and the functional blocks for the re-transmission at f_1 (yellow). The PMU includes a full-wave passive rectifier [24] equipped with V_{th}-cancellation [25] (Figure 5(a)) and two Low Dropout Regulators (LDOs) to supply respectively the Phased Locked Loop (PLL) at V_{reg0} = 1.8 V and the Power Amplifier (PA) at V_{reg1} = 3 V (Figure 5(b)). The error amplifier of each LDO (Figure 5(b)) is a single-stage operational transconductance amplifier. The PLL (Figure 5(c)) operates from the lower f_0 with a x32 divider in feedback within the phase frequency detector, the charge pump and the voltage controlled oscillator. f_1 is re-transmitted via SR_1 through the class-E PA (Figure 5(d)).

Figure 6 shows the simulation of the main circuits of the CMOS IC in Figure 5 with the aim of proving its feasibility while analyzing the power losses in the circuitry (η_{IC}). The full-wave rectifier shows a stable Power Conversion Efficiency (PCE) higher than 60% for input powers in the FS-IPT range of interest (several hundreds of mW received at SR_0) and for small impedance loads R_L (tens of ohms as required for transmitting few hundreds of mW from SR_1). In particular, a peak PCE of 75% is highlighted for an input power of 520 mW and for R_L = 50 Ω (Figure 6(a), blue) together with a rectified voltage of 5.2 V (Figure 6(b), blue). Figure 6(c) shows the transient line regulation behaviour of the two designed LDOs respectively for supplying the PLL at V_{reg0} = 1.8 V (blue) and the PA at V_{reg1} = 3 V (orange). Both LDOs are characterised by a quiescent current of 200 μA consuming a total power of 744 μW. Figure 6(d), (e) show respectively the transient behaviour and its magnification of the PMU start-up while supplying the frequency switching circuitry by the PLL. The latter is supplied at V_{reg0} (purple) and converts the squared-buffered input SR_0 signal at f_0 = 13.56 MHz (orange) to the squared f_1 = 433.92 MHz (yellow) consuming 809.6 μW. Finally, the fully on-chip class-E PA delivers 200 mW through SR_1 (Figure 6(f)) with an efficiency η_{PA} = 58.5%.

Considering the circuitry of Figure 5 and neglecting the LDOs and PLL power consumption (i.e., order of magnitude smaller compared to the rectifier and the PA), η_{IC} of (5) is

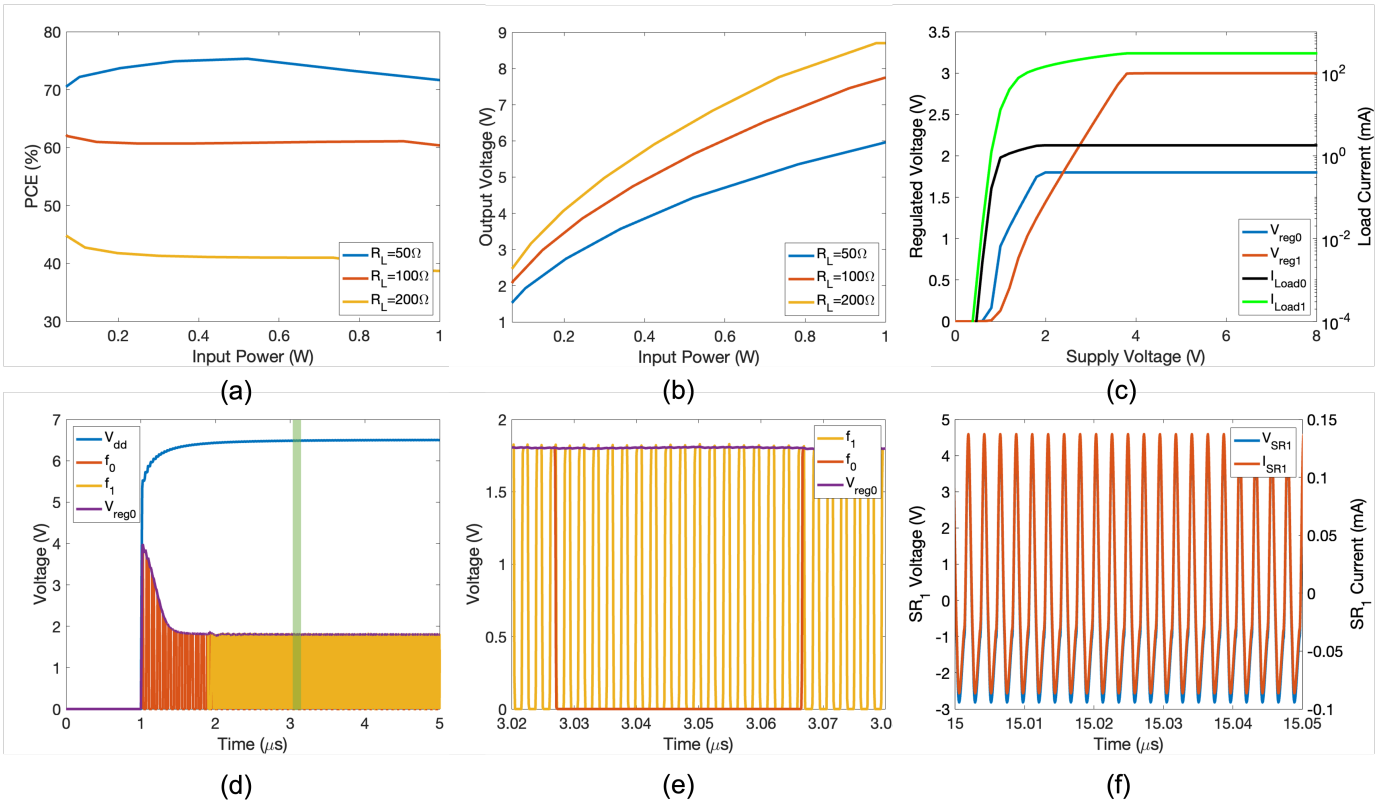

Figure 6. Simulations of the main functional circuits of the CMOS IC for frequency switching. Rectifier (a) PCE and (b) output voltage as a function of the input power at f_0=13.56 MHz for loads of 50Ω (blue), 100Ω (orange) and 200Ω (yellow). Regulated voltage and current (V_{reg0}, I_{Load0} for LDO_0 - blue, black; and V_{reg1}, I_{Load1} for LDO_1 - orange, green) as a function of the un-regulated rectified supply voltage. (c) Transient operation of the PMU and PLL supplied at V_{reg0} (purple) for switching the frequency from f_0 (orange) to f_1 (yellow). (d) Green strip magnification highlighting the squared f_1 (yellow) at 433.92 MHz. (e) Output voltage (blue) and current (orange) delivered by SR_1 at f_1 through the class-E PA.

approximated as $\eta_{IC} \simeq$ PCE·$\eta_{PA} \simeq 41\%$.

B. FS-IPT Characterisation

Table I summarizes the simulated and measured features of the FS-IPT link including the main geometrical characteristics and the physical parameters constituting each coil.

Figure 7(a), (b), (c) show the ex-vivo measurement setup respectively from top, side and bottom view highlighting the Tx and the active resonator including SR_0, SR_1 and 37 Res.

Figure 7(d)-(g) show the simulated (dashed) and measured (continuous) real (red) and imaginary (blue) impedances of the matched coils constituting the FS-IPT link, highlighting a perfect resonance frequency match. In particular, Tx (Figure 7(d)) and SR_0 (Figure 7(e)) resonate at f_0 = 13.56 MHz while SR_1 (Figure 7(f)) and Res (Figure 7(g)) resonate at f_1 = 433.92 MHz. Small amplitude discrepancies are related to the ideal matching networks used in the simulations.

The Tx-SR_0 link works at the resonating frequency of f_0 = 13.56 MHz and presents similar characteristics to previous works [32]. In particular, PTE_0 = 23% at a working distance of 14 mm. It is worth to notice that in the FS-IPT system, the low-frequency Tx-SR_0 link does not limit the power requirements of the high-frequency link. For example, when P_S = 2.17 W, PDL_0 = 500 mW with a maximum SAR of 0.013 W/kg at skin level (i.e., more than two orders of magnitude smaller with respect to maximum allowable SAR). Therefore, the source power P_S can be adjusted based on the Rx power requirements. As an example, for an implant requiring 300 μW at Rx side, a minimum of 200 mW needs to be transmitted by SR_1 obtaining a maximum SAR of 0.84 W/kg at brain level for the high-frequency transmission (i.e., substantially higher with respect to the low-frequency SAR while still far below the safety limits).

Considering the efficiencies of the low-frequency (PTE_0 = 23%) and high-frequency (PTE_1 = 0.14%) links and the simulated η_{IC} = 41% for the CMOS IC of Figure 5, the total PTE for the FS-IPT is 0.013%, as in (5). In this scenario, the Rx receives 300 μW from a P_S = 2.17 W. The same external source power with a traditional three-coil IPT link allows a maximum SAR-constrained PDL of 15 μW.

V. Discussion

Table II compares this work against the state-of-the-art. A distinction is made between studies relying on measures from fabricated devices (top) and studies based on simulations (bottom). A first comparison is done through FOM_1 [33] as

Table I: SPECIFICATIONS OF THE FS-IPT LINK.

	Parameter	Simulation	Measurement
Tx	L (nH) at f_0	56.1	56.7
	R (Ω) at f_0	0.07	0.07
	Q at f_0	67.6	64.4
	SRF (MHz)	511.3	559.1
	C_p (nF)	6.8	6.7
	C_s (nF)	5.7	3.7
	D_o (mm)	16	
	n	2	
	w (mm)	1.5	
	s (mm)	1	
	t (μm)	50	
SR_0	L (nH) at f_0	38	40.3
	R (Ω) at f_0	0.08	0.12
	Q at f_0	43.4	27.3
	SRF (MHz)	827.9	1236
	C (nF)	5.8	4.5
	D_o (mm)	13.5	
	n	1	
	w (mm)	0.5	
	s (mm)	N/A	
	t (μ m)	18	
SR_1	L (nH) at f_1	93.2	78
	R (Ω) at f_1	4.32	3.8
	Q at f_1	58.7	56
	SRF (MHz)	727.1	1065.6
	C (pF)	1.8	2.4
	D_o (mm)	14.7	
	n	1	
	w (mm)	0.06	
	s (mm)	N/A	
	t (μm)	18	
Res	L (nH) at f_1	14.4	12.3
	R (Ω) at f_1	0.4	0.4
	Q at f_1	98.1	81.6
	SRF (GHz)	4.1	3.4
	C (pF)	32.2	28.5
	D_o (mm)	2.4	
	n	1	
	w (mm)	0.1	
	s (mm)	N/A	
	t (μm)	35	

in (7):

$$FOM_1 = \frac{PTE \cdot d^3}{A_{Rx}^{1.5}} \tag{7}$$

Since FOM_1 does not consider the safety constrains of the IPT link, a second comparison is introduced through FOM_2. It includes the SAR-constrained PDL at the numerator in place of the PTE, as in (8):

$$FOM_2 = \frac{(SAR-constrained-PDL) \cdot d^3}{A_{Rx}^{1.5}} \tag{8}$$

In both the cases, the FS-IPT outperforms the other methods. For all the IPT links of Table II, a key element is the

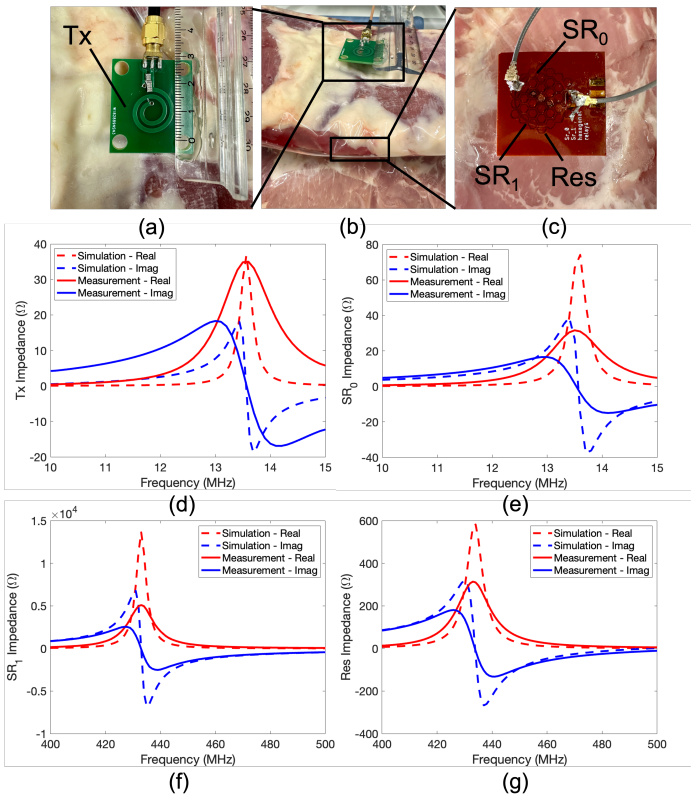

Figure 7. Experimental ex-vivo setup for the coils characterisation: (a) top-view highlighting the Tx, (b) side-view and (c) bottom-view highlighting the active resonator including SR_0, SR_1 and 37 Res. Comparison among the measured (continuous line) and simulated (dashed lines) real (red) and imaginary (blue) impedance of the (d) Tx, (e) SR_0, (f) SR_1 and (g) Res coils constituting the FS-IPT link.

interplay between the operating frequency and the Rx size. For millimetric size Rx the operating frequency is in the order of few tens of MHz [30], [21] and never exceed 250 MHz [31]. When the Rx size decreases, the operating frequency increases accordingly. Similarly, when the frequency is relatively low the SAR-constrained PDL is high (and FOMs are high). With a 50 MHz and 60 MHz carrier frequencies, a maximum PDL of 2370 μW and 1300 μW is respectively obtained [30], [21]. On the other hand, with higher frequencies of 915 MHz and 1.18 GHz the maximum PDL decreases to 235 μW [27] and 55.5 μW [9] with the SAR exceeding the safety limit (respectively 19.6 W/kg and 30.6 W/kg). Hence, duty-cycling the RF transmission is necessary for these approaches. The FS-IPT link takes advantages of the low-frequency link to transmit higher power for the long distance (Tx-SR_1 distance) and of the high-frequency to transmit power to the Rx for the short distance (SR_1-Rx). This way, the maximum PTE_1 increases by almost two order of magnitudes while the maximum SAR-constrained PDL increases by more than six decades compared to the state-of-the-art. Hence, the FS-IPT removes the need of duty-cycling the RF transmission and enables continuous operation of miniaturised neural implants. Moreover, the FS-IPT link retains all the advantages of the standard three-coil

Table II:
STATE-OF-THE-ART INDUCTIVE LINKS COMPARISON.

	Ref., IPT Link	Rx Size (mm^3)	Freq. (MHz)	Distance (mm)	PTE (%)	PDL (μW)	R_{Load} (Ω)	SAR (W/kg)	Rx Num.	FOM_1	FOM_2
Measurements	[26], 2C	1x1x1	200	12	0.56	224	5000	1.6	1	967	0.38
	[21], 3C	1x1x1	60	16	2.4	1300	500	1.6	N/A	9830	5.3
	[27], 3C	0.5x0.5x0.0034	915	8	0.047	235	N/A	19.6	1000	192	0.07
	[28], 2C	0.25x0.5x0.004	1500	1	0.021	10.5	N/A	N/A	1	0.47	N/A[#]
	[9], 2C	0.3x0.3x0.004	1180	6.6	0.0019*	55.5	50	30.6	N/A	20.2	0.031
	[29], 2C	0.1x0.1xN/A	2000	1.2	0.0016	100	N/A	N/A	1	2.8	N/A[#]
Simulations	[30], 2C	1x1x1	50	10	2.2	2370	N/A	1.6	1	2200	2.37
	[31], 2C	1x1x1	250	16	6.8	76.4	N/A	1.6	1	27852	0.31
	This Work, 3C	0.2x0.2x0.002	433	14	0.0018	32	3000	1.6	1024	617	10.9
	This Work, FS	**0.2x0.2x0.002**	**13.56/433**	**14**	**0.013**	**1970**	**3000**	**1.6**	**1024**	**4459**	**675.7**

2C: two-coil; 3C: three-coil. *Rectifier included. [#]SAR not available (PDL only).

IPT link, such as the capability to power multiple Rx at the same time. It is also worth to mention that when multiple Res are coupled with SR_1 the frequency splitting phenomena is occurring [14]. The latter can be mitigated using current sources (instead of voltage ones) to drive the transmitting stage and developing series resonant tanks [14]. In addition, the frequency splitting phenomena could be used to increase the communication bandwidth [34]. Additionally, due to the improved SAR-constrained PDL, the FS-IPT is a promising solution for exploiting further miniaturisation of the Rx, for which the low efficiency and the safety constrains are key limiting factors within traditional inductive links.

Finally, the full potential of the FS-IPT link is its scalability. This work presented a system to power 1024 implants in a total area of 163.84 mm^2. However, if we consider the active resonator and the 1024 (or any generic n) Rx chips as a module, multiple M modules can be implanted in different brain areas, each of them working from the same low frequency f_0 to different high frequencies f_1, f_2, ..., f_M, each generated by the circuit responsible for the frequency switching (Figure 8). It has been demonstrated that by selecting a specific resonating capacitance to different miniaturised implants it is possible to exploit the Frequency Division Multiple Access together with a phased array transmitting system to individually power via IPT different Rx with different frequency spans [9], [35]. For example, with a resonating frequency span of 100 MHz, 8 different modules can be controlled in the high frequency range from the smaller 433 MHz (as in this work) to the higher

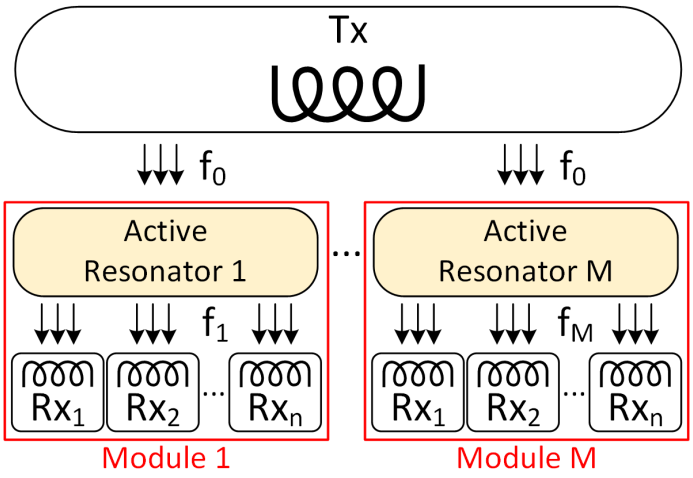

Figure 8. Scalability of the FS-IPT system considering M parallel modules each receiving power at low frequency f_0 from the common Tx and delivering power to n Rx each at a different frequency from f_1 to f_M.

1.13 GHz. With 8 modules and 1024 implants per module a total of 8192 implants distributed over a large brain area can be powered with the FS-IPT link. This opens new scenarios towards wireless, miniaturised and large-scale brain-machine interfaces, such as cortical visual prostheses [36].

VI. Conclusion

In this work the FS-IPT link has been introduced. The novel system has been simulated and optimised considering a subdural active resonator capable of wirelessly power 1024 miniaturised chips by switching the operating frequency from a low carrier for the skin-dura transmission to an higher frequency for the dura-brain link, substantially decreasing the maximum SAR. Despite the added design complexity, preliminary results suggest the FS-IPT as a promising alternative to state-of-the-art three-coil inductive links by improving the maximum efficiency by almost two order of magnitude and the maximum delivered power by more than six decades. The FS-IPT link could be scaled up by combining different parallel modules to increase the number of channels, thus motivating further investigations for the development of wireless, miniaturised and large-scale brain-machine interfaces.

VII. Acknowledgement

This project is supported by a generous foundation represented by CARIGEST SA and by the Interdisciplinary Seed Fund from École Polytechnique Fédérale de Lausanne. The Authors would like to thank Mr. Ali Abdul Ameer Abbas, Mr. Yiming Wei and Mr. Fabrizio Grani for their help.

References

[1] K. M. Szostak et al. "Distributed Neural Interfaces: Challenges and Trends in Scaling Implantable Technology". In: *Handbook of Neuroengineering* (2021), pp. 1–37.

[2] A. Nurmikko. "Challenges for large-scale cortical interfaces". In: *Neuron* 108.2 (2020), pp. 259–269.

[3] G. L. Barbruni et al. "Miniaturised wireless power transfer systems for neurostimulation: A review". In: *IEEE Transactions on Biomedical Circuits and Systems* 14.6 (2020), pp. 1160–1178.

[4] G. L. Barbruni, D. Ghezzi, and S. Carrara. "Challenges for Miniaturized Neurostimulators: Design of wireless Bio/CMOS interfaces for brain stimulation". In: *IEEE Solid-State Circuits Magazine* 15.2 (2023), pp. 34–40.

[5] M. Kiani, U.-M. Jow, and M. Ghovanloo. "Design and optimization of a 3-coil inductive link for efficient wireless power transmission". In: *IEEE transactions on biomedical circuits and systems* 5.6 (2011), pp. 579–591.

[6] 2. IEEE Standards Coordinating Committee. "IEEE standard for safety levels with respect to human exposure to radio frequency electromagnetic fields, 3kHz to 300GHz." In: *IEEE C95.* (1992), pp. 1–1991.

[7] A. Christ et al. "Assessing human exposure to electromagnetic fields from wireless power transmission systems." In: *Proceedings of the IEEE.* 101.6 (2013), pp. 1482–1493.

[8] A. S.Y. Poon, S. O'Driscoll, and T. H. Meng. "Optimal frequency for wireless power transmission into dispersive tissue". In: *IEEE Transactions on Antennas and Propagation* 58.5 (2010), pp. 1739–1750.

[9] A. Khalifa et al. "The Microbead: A 0.009 mm 3 Implantable Wireless Neural Stimulator." In: *IEEE transactions on biomedical circuits and systems* 13.5 (2019), pp. 971–985.

[10] J. Lee et al. "Neural recording and stimulation using wireless networks of microimplants". In: *Nature Electronics* 4.8 (2021), pp. 604–614.

[11] P. Feng and T. G. Constandinou. "Robust wireless power transfer to multiple mm-scale freely-positioned neural implants". In: *2018 IEEE Biomedical Circuits and Systems Conference (BioCAS)*. IEEE. 2018, pp. 1–4.

[12] J. Pepper et al. "The risk of hardware infection in deep brain stimulation surgery is greater at impulse generator replacement than at the primary procedure". In: *Stereotactic and functional neurosurgery* 91.1 (2013), pp. 56–65.

[13] M. Meng and M. Kiani. "A hybrid inductive-ultrasonic link for wireless power transmission to millimeter-sized biomedical implants". In: *IEEE Transactions on Circuits and Systems II: Express Briefs* 64.10 (2016), pp. 1137–1141.

[14] P. Perez-Nicoli, F. Silveira, and M. Ghovanloo. "Inductive Links for Wireless Power Transfer". In: *Springer* (2021).

[15] U.-M. Jow and M. Ghovanloo. "Design and optimization of printed spiral coils for efficient transcutaneous inductive power transmission". In: *IEEE Transactions on biomedical circuits and systems* 1.3 (2007), pp. 193–202.

[16] M. Kiani and M. Ghovanloo. "A figure-of-merit for designing high-performance inductive power transmission links". In: *IEEE transactions on industrial electronics* 60.11 (2012), pp. 5292–5305.

[17] P. Feng et al. "Chip-scale coils for millimeter-sized bio-implants". In: *IEEE transactions on biomedical circuits and systems* 12.5 (2018), pp. 1088–1099.

[18] S. Gabriel, R.W. Lau, and C. Gabriel. "The dielectric properties of biological tissues: III. Parametric models for the dielectric spectrum of tissues". In: *Physics in medicine & biology* 41.11 (1996), p. 2271.

[19] A. Drossos, V. Santomaa, and N. Kuster. "The dependence of electromagnetic energy absorption upon human head tissue composition in the frequency range of 300-3000 MHz". In: *IEEE transactions on microwave theory and techniques* 48.11 (2000), pp. 1988–1995.

[20] P.K. Campbell et al. "A silicon-based, three-dimensional neural interface: manufacturing processes for an intracortical electrode array". In: *IEEE Transactions on Biomedical Engineering* 38.8 (Aug. 1991), pp. 758–768. ISSN: 1558-2531. DOI: 10.1109/10.83588.

[21] S. A. Mirbozorgi, P. Yeon, and M. Ghovanloo. "Robust wireless power transmission to mm-sized free-floating distributed implants." In: *IEEE transactions on biomedical circuits and systems* 11.3 (2017), pp. 692–702.

[22] F. Merli et al. "The effect of insulating layers on the performance of implanted antennas." In: *IEEE Transactions on Antennas and propagation* 59.1 (2010), pp. 21–31.

[23] E. Borda et al. "Conformable neural interface based on off-stoichiometry thiol-ene-epoxy thermosets". In: *Biomaterials* 293 (2023), p. 121979.

[24] M. Kiani et al. "A Q-modulation technique for efficient inductive power transmission". In: *IEEE journal of solid-state circuits* 50.12 (2015), pp. 2839–2848.

[25] T. T Le et al. "Piezoelectric micro-power generation interface circuits". In: *IEEE journal of solid-state circuits* 41.6 (2006), pp. 1411–1420.

[26] D. Ahn and M. Ghovanloo. "Optimal design of wireless power transmission links for millimeter-sized biomedical implants." In: *IEEE transactions on biomedical circuits and systems* 10.1 (2016), pp. 125–137.

[27] J. Lee et al. "An implantable wireless network of distributed microscale sensors for neural applications." In: *2019 9th International IEEE/EMBS Conference on Neural Engineering (NER)* (Mar. 2019), pp. 871–874.

[28] W. Biederman et al. "A Fully-Integrated, Miniaturized (0.125 mm²) 10.5 μW Wireless Neural Sensor." In: *IEEE Journal of Solid-State Circuits* 48.4 (2013), pp. 960–970.

[29] N. C. Kuo, B. Zhao, and A. M. Niknejad. "Equation-based optimization for inductive power transfer to a miniature CMOS rectenna." In: *IEEE Transactions on Microwave Theory and Techniques* 66.5 (2018), pp. 2393–2408.

[30] A. Ibrahim and M. Kiani. "Safe inductive power transmission to millimeter-sized implantable microelectronics devices." In:

Int. Conf. IEEE Engineering in Medicine and Biology Society (EMBC) (2015), pp. 817–820.

[31] E. Moradi et al. "Antenna design for implanted tags in wireless brain machine interface system." In: *2013 IEEE Antennas and Propagation Society International Symposium (APSURSI)* (July 2013), pp. 2083–2084.

[32] U.-M. Jow and M. Ghovanloo. "Modeling and optimization of printed spiral coils in air, saline, and muscle tissue environments". In: *IEEE transactions on biomedical circuits and systems* 3.5 (2009), pp. 339–347.

[33] M. Zargham and P. G. Gulak. "Fully Integrated On-Chip Coil in 0.13um CMOS for Wireless Power Transfer Through Biological Media". In: *IEEE transactions on biomedical circuits and systems* 9.2 (2014), pp. 259–271.

[34] Y. Park et al. "A wireless power and data transfer IC for neural prostheses using a single inductive link with frequency-splitting characteristic". In: *IEEE Transactions on Biomedical Circuits and Systems* 15.6 (2021), pp. 1306–1319.

[35] A. Khalifa et al. "The microbead: A highly miniaturized wirelessly powered implantable neural stimulating system". In: *IEEE transactions on biomedical circuits and systems* 12.3 (2018), pp. 521–531.

[36] D. Ghezzi. "The role of the visual field size in artificial vision". In: *Journal of Neural Engineering* 20.2 (2023), p. 023001.

Gian Luca Barbruni was born in Sanremo (IM), Italy in 1995. He received both the B.Sc. and M.Sc. degrees in Biomedical Engineering from the Politecnico di Torino, Turin, Italy in 2017 and 2019 respectively. He was a Research Associate at the Department of Electronic Engineering (DET) and MiNES (Micro&Nano Electronic Systems) Laboratory at Politecnico di Torino. Actually he is conducting his Ph.D. in Microsystems and Microelectronics (EDMI) at École Polytechnique Fédérale de Lausanne - Microcity, Neuchâtel, Switzerland. His project is focused on the development of miniaturised neuroprosthesis device for artificial vision. His current research interests include neural prosthesis, biosensors, wireless power transfer and data communication, ultra-low-power and miniaturised CMOS integrated circuits for the development of innovative biomedical systems.

Claudia Cordara was born in Milano, Italy, in 1998. She received both the B.Sc. and M.Sc. degrees in Biomedical Engineering at Politecnico di Milano, in 2020 and 2023 respectively. She conducted her master thesis project at the École Polytechnique Fédérale de Lausanne - Microcity, Neuchâtel, Switzerland, working on the development of a novel frequency-shifting inductive link for wireless power transmission to miniaturised neural implants.

Marco Carminati (M'07, SM'18) is Associate Professor at Politecnico di Milano (Italy) and affiliated with the Italian National Institute of Nuclear Physics (INFN). He received B.Sc. (2003), M.Sc. (2005) magna cum laude and Ph.D. (2010) degrees in Electronics Engineering from Politecnico di Milano, where he was post-doc (2010-2016) and Assistant Professor (2016-2021). He serves as Secretary of the Italy Chapter of the IEEE Nuclear and Plasma Science Society. Dr. Carminati also serves as Associate Editor of IEEE TAFE and TBioCAS with interests in low-noise electronics for micro-sensors and radiation detectors, with applications to physics, medicine and environmental monitoring. He has authored and co-authored more than 250 peer-reviewed scientific publications.

Sandro Carrara (F'15) is an IEEE Fellow and also the recipient of the IEEE Sensors Council Technical Achievement Award. He is a professor and head of the Bio/CMOS Interfaces Laboratory at the EPFL in Lausanne (CH). He is a former professor at the Universities of Genoa and Bologna (IT). He holds a Ph.D. in Biochemistry and Biophysics from the University of Padua (IT), a Master degree in Physics from the University of Genoa (IT), and a diploma in Electronics from the National Institute of Technology in Albenga (IT). Along his carrier, he published 7 books with prestigious publishers such as Springer/NATURE and Cambridge University Press. He has more than 380 scientific publications and is author of 17 patents. He is Editor-in-Chief of the IEEE Sensors Journal, one of the largest journals among 220 IEEE publications, and Associate Editor of the IEEE Transactions on Biomedical Circuits and Systems. He is a member of the IEEE Sensors Council and its Executive Committee. He was in the Board of Governors (BoG) of the IEEE CAS Society.

Diego Ghezzi received his M.Sc. in Biomedical Engineering (2004) and Ph.D. in Bioengineering (2008) from Politecnico di Milano. From 2008 to 2013, he completed his postdoctoral training at Istituto Italiano di Tecnologia in Genova at the Department of Neuroscience and Brain Technologies, where he was promoted to Researcher in 2013. In 2015, he was appointed Assistant Professor of Bioengineering with the Medtronic Chair in Neuroengineering at the Center for Neuroprosthetics and Institute of Bioengineering of the École Polytechnique Fédérale de Lausanne. Since 2023, he is direct of surgical technologies and innovations at the Hôpital ophtalmique Jules-Gonin in Lausanne. His laboratory (Ophthalmic and Neural Technologies laboratory) is a multidisciplinary environment promoting cross-fertilization among diverse expertise. It brings materials science, engineering, computer science, life science, and medicine together by the convergence of physicists, engineers, neuroscientists, and ophthalmologists cooperating to accomplish innovative projects. The mission is to develop innovative ophthalmic and neural technologies to better understand diseases and, eventually, improve the quality of life of people with ophthalmic and neural disorders. Ultimately, we aim at translating our research findings into clinical practice.